Monte Carlo simulation of terahertz quantum cascade laser structures based on wide-bandgap semiconductors

Enrico Bellotti,[a] Kristina Driscoll,[b] Theodore D. Moustakas, and Roberto Paiella
Department of Electrical and Computer Engineering and Photonics Center, Boston University, 8 Saint Mary's Street, Boston, Massachusetts 02215, USA

(Received 4 February 2009; accepted 23 April 2009; published online 2 June 2009)

Wide-bandgap semiconductors such as GaN/AlGaN and ZnO/MgZnO quantum wells are promising for improving the spectral reach and high-temperature performance of terahertz quantum cascade lasers, due to their characteristically large optical phonon energies. Here, a particle-based Monte Carlo model is developed and used to quantify the potential of terahertz sources based on these materials relative to existing devices based on GaAs/AlGaAs quantum wells. Specifically, three otherwise identical quantum cascade structures based on GaN/AlGaN, ZnO/MgZnO, and GaAs/AlGaAs quantum wells are designed, and their steady-state carrier distributions are then computed as a function of temperature. The simulation results show that the larger the optical phonon energies (as in going from the AlGaAs to the MgZnO to the AlGaN materials system), the weaker the temperature dependence of the population inversion. In particular, as the temperature is increased from 10 to 300 K, the population inversions are found to decrease by factors of 4.48, 1.50, and 1.25 for the AlGaAs, MgZnO, and AlGaN structure, respectively. Based on these results, the AlGaN and MgZnO devices are then predicted to be in principle capable of laser action without cryogenic cooling. © *2009 American Institute of Physics*. [DOI: 10.1063/1.3137203]

I. INTRODUCTION

The terahertz spectral region, often defined as the frequency range between 300 GHz and 10 THz (i.e., the wavelength range between 1 mm and 30 μm), has so far remained largely unutilized due to the lack of practical sources and detectors.[1] This spectral range—sometimes referred to as the "terahertz gap"—lies at the intersection between the traditional domains of electronics and photonics, where many of the conventional device concepts and techniques used in either domain fail to provide the required levels of performance. On the other hand terahertz technologies are promising for many sensing, spectroscopy, and imaging applications, related to the ability of terahertz light to penetrate through many packaging materials with little attenuation, and to the presence of distinctive rotational/vibrational resonances at terahertz frequencies in many complex molecules of interest. These favorable properties have motivated extensive research in the past several years aimed at the development of the required components and at the demonstration of a wide range of applications of terahertz light, e.g., for security screening, manufacturing quality control, and medical diagnostics.

Similar to the case of other spectral regions, the widespread emergence of these terahertz-based technologies will require the development of practical semiconductor devices for the generation, processing, and detection of terahertz light. In the area of sources, an important milestone has been reported in 2002 with the demonstration of the first terahertz semiconductor laser based on the quantum cascade (QC) scheme.[2] In this lasing modality, light emission involves intersubband (ISB) transitions in quantum wells (QWs)—i.e., electronic transitions between quantized states within the same energy band[3]—so that the emission wavelength can be tuned over a broad spectral range through the design of the QW active material. Since 2002, terahertz QC lasers based on GaAs/AlGaAs QWs have made remarkable progress[4–8] and can now cover the frequency range between 1.2 and 5 THz, often with output powers of several milliwatts. As such, they have emerged as a very attractive technology for many of the aforementioned applications.

At the same time, however, the operation of these GaAs/AlGaAs devices fundamentally requires cryogenic cooling, with maximum temperatures reported so far near 170 and 120 K for pulsed and continuous-wave emission, respectively.[5] Furthermore, their present wavelength coverage cannot be extended much further into the high-frequency side of the terahertz region. Both of these limitations are intrinsic, as they are related to the presence in (Al)GaAs of optical phonon modes with terahertz frequencies (e.g., $\nu_{LO} \approx 8.2$ THz in GaAs). The excitation of these vibrational modes provides both a prohibitively large absorption mechanism for light at the same frequencies (reststrahlen absorption) and an ultrafast nonradiative decay mechanism between laser subbands separated by terahertz-range energies. As a result, GaAs-based devices are completely precluded from operation at frequencies within and immediately around the ~8–9 THz GaAs reststrahlen band. GaAs/AlGaAs QC lasers emitting at lower frequencies ν can be realized but are limited to operation at cryogenic temperatures, due to the process of thermally activated LO-phonon emission.

This nonradiative decay mechanism is illustrated schematically in Fig. 1, where we plot the dispersion curves (en-

[a]Electronic mail: bellotti@bu.edu.
[b]Current address: Cavendish Laboratory, Cambridge University, Cambridge CB3 0HE, England.

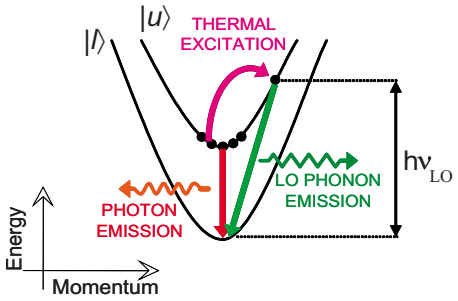

FIG. 1. (Color online) Schematic illustration of the competition between photon emission and thermally activated LO-phonon emission by electrons in the upper laser subband of a terahertz QC structure.

ergy versus in-plane wavenumber k) of the upper and lower laser subbands (labeled $|u\rangle$ and $|l\rangle$, respectively) of a generic terahertz QC structure. Laser action in this active material involves the selective injection of electrons in the upper subband $|u\rangle$. At cryogenic temperatures, the majority of these electrons occupy states near the bottom of the subband, from which they cannot decay nonradiatively into $|l\rangle$ via LO-phonon emission if $\nu < \nu_{\mathrm{LO}}$, because of the requirement of energy conservation; as a result, a large population inversion can be established. As the temperature is increased, however, more and more of the electrons in $|u\rangle$ gain enough thermal energy that scattering into $|l\rangle$ via LO-phonon emission becomes allowed. Since these scattering processes are ultrafast, the end result is a dramatic reduction in the device population inversion and optical gain. A recent experimental study has indicated that this mechanism is indeed the main factor limiting the operation of GaAs/AlGaAs terahertz QC lasers to cryogenic temperatures.[6]

It follows from this argument that the closer the laser emission frequency ν to the LO-phonon frequency ν_{LO} of the QW materials, the more effectively the population inversion is degraded with increasing temperature. In particular, terahertz QC-laser action at room temperature T_{rt} will likely require that the energy difference $h\nu_{\mathrm{LO}} - h\nu$ be significantly larger than the thermal energy $k_B T_{\mathrm{rt}} \approx 26$ meV, so that LO-phonon-assisted nonradiative decay from $|u\rangle$ to $|l\rangle$ is disallowed even to (most) thermally excited electrons in $|u\rangle$. In GaAs wells, where $h\nu_{\mathrm{LO}} \approx 36$ meV, the above condition is not fully satisfied at any terahertz emission frequency. Therefore, it is likely that further progress in the high-temperature performance of terahertz injection lasers will require novel heterostructures featuring larger LO-phonon frequencies. Suitable materials may be found among wide-bandgap semiconductors, which are commonly characterized by strongly ionic chemical bonds. Consequently, the relative displacement of neighboring atoms in these materials is opposed by particularly large electrostatic restoring forces, leading to optical modes of lattice vibrations with particularly high oscillation frequencies.

A promising materials system in this respect is that of GaN/AlGaN QWs, where the LO-phonon energies lie in the 91–99 meV range. ISB absorption, photodetection, and photoluminescence in these QWs have been measured and investigated in recent years,[9–16] particularly at near-infrared wavelengths as allowed by the record large conduction-band offset of the GaN/AlN interface (about 1.75 eV). A number of theoretical studies have also considered the design of GaN/AlGaN terahertz QC lasers[17–19] and pointed out how these devices could in principle close out the spectral gap left behind by arsenide-based terahertz sources as well as provide improved high-temperature performance. In particular, in Ref. 19, a Monte Carlo analysis was carried out to directly compare two QC structures based on the same design scheme and with the same target emission frequency, consisting of GaAs/AlGaAs and GaN/AlGaN QWs, respectively. With this approach, a rigorous quantitative estimate of the potential for improvement offered by the latter system was obtained.

Here we provide a detailed description of the Monte Carlo model used in the simulations of Ref. 19, and we present additional numerical results to further illustrate the model capabilities and substantiate its conclusions. In addition, we consider a second family of wide-bandgap large-LO-phonon-energy semiconductors as a potential candidate for terahertz ISB optoelectronics, namely, ZnO/MgZnO QWs. These heterostructures are also currently the subject of extensive research, primarily aimed at the development of ultraviolet light emitting diodes and lasers based on excitonic interband transitions. Compared to GaN/AlGaN QWs, their material and device technology is in an even earlier stage, although some potential advantages have been suggested including generally smaller lattice mismatch and weaker polarization fields. The main drawback, i.e., the difficulties associated with p-type doping, is irrelevant in the present context. Nevertheless, ISB transitions in ZnO/MgZnO QWs have only been measured in one recent report,[20] where photocurrent spectroscopy was used to identify ISB absorption peaks at midinfrared wavelengths. Because of their large LO-phonon energies (72 meV in ZnO), these materials are also ultimately promising for the development of terahertz QC lasers, and their inclusion in this study is partly aimed at motivating exploratory experimental efforts in this direction. From a QC-laser-physics standpoint, it also provides an additional data point to elucidate the relationship between high-temperature terahertz laser characteristics and the LO-phonon energies of the underlying active materials.

This article is organized as follows. In Sec. II, we present the gain medium design of three nominally "identical" terahertz QC structures based on the aforementioned materials systems (i.e., GaAs/AlGaAs, GaN/AlGaN, and ZnO/MgZnO QWs). Section III is devoted to the Monte Carlo simulation model used to study carrier dynamics in these structures. Key features of this model are the inclusion of electron/LO-phonon and electron/electron scattering and the treatment of screening based on a temperature-dependent single-subband approach, and all the relevant formulas are presented and discussed in detail. In Sec. IV, this Monte Carlo model is used to compute the steady-state carrier distributions of the three QC structures under study as functions of temperature. Illustrative plots of the calculated distributions are presented, together with the resulting fractional population inversions versus temperature. The latter results are finally used to estimate the maximum operation temperatures of the three devices, which clearly highlight the poten-

tial of wide-bandgap materials for terahertz QC-laser applications. The article then concludes with a brief discussion of the technological challenges involved in the experimental demonstration of these new devices.

II. DEVICE DESIGN

The QC gain media studied in this work were designed using a Schrödinger-equation solver based on the effective-mass approximation. Their conduction-band profiles under optimal bias conditions are plotted in Figs. 2(a)–2(c), together with the squared envelope functions of the relevant bound states (referenced to their respective energy levels). Specifically, these structures consist of GaAs/$Al_{0.15}Ga_{0.85}As$, GaN/$Al_{0.15}Ga_{0.85}N$, and ZnO/$Mg_{0.15}Zn_{0.85}O$ well/barrier combinations, respectively. In the former case, the barrier composition was chosen in accordance with most experimental demonstrations of GaAs terahertz QC lasers reported so far.[2,4–8] In the case of the GaN and ZnO structures, it was selected to produce a similar degree of quantum confinement of the subbands involved in the laser action. In particular, the energy separation between the manifold of excited states $|2\rangle$-$|4\rangle$ in each repeat unit and the *average* conduction-band edge of the injection barrier downstream is approximately the same in all three structures, around 50–60 meV. By coincidence, this criterion is consistent with the same concentration (15%) of the additional element in the barrier alloy. The layer thicknesses of a single repeat unit, starting from the injection barrier (indicated by the arrow) and moving downstream, are **49**/94/**33**/74/**56**/156 for the GaAs structure, **26**/37/**22**/31/**26**/59 for the GaN structure, and **30**/31/**25**/24/**34**/55 for the ZnO structure, where the bold numbers refer to the barrier layers. The externally applied electric field F_{ext} in each plot is selected to produce a situation of near anticrossing between the lowest subband $|1\rangle$ of each repeat unit and subband $|4\rangle$ of the unit downstream. The specific values are 11, 73, and 48 kV/cm for the GaAs, GaN, and ZnO devices, respectively.

In order to obtain the fairest possible comparison between the materials systems under consideration, these three gain media were designed based on the same scheme, i.e., a variation of the "resonant-phonon" terahertz QC design[5] involving only three QWs per repeat unit.[7] The optical transitions occur between the subbands labeled $|4\rangle$ and $|3\rangle$ in each repeat unit of the active materials. The lower laser states are rapidly depopulated through tunneling into state $|2\rangle$ downstream and scattering into state $|1\rangle$ via resonant LO-phonon emission. To maximize the speed of the latter process, the energy separation between subbands $|2\rangle$ and $|1\rangle$ is close to the LO-phonon energy of the well material. At the same time, the spatial overlap between states $|4\rangle$ and $|1\rangle$ in each repeat unit is kept as small as possible, to avoid fast depopulation of the latter (at least at low temperatures). This QC design scheme has been successfully demonstrated with a recent GaAs/AlGaAs device,[7] and was chosen for this study because of its inherent simplicity. Also for the sake of a fair comparison, the three gain media of Fig. 2 feature the same

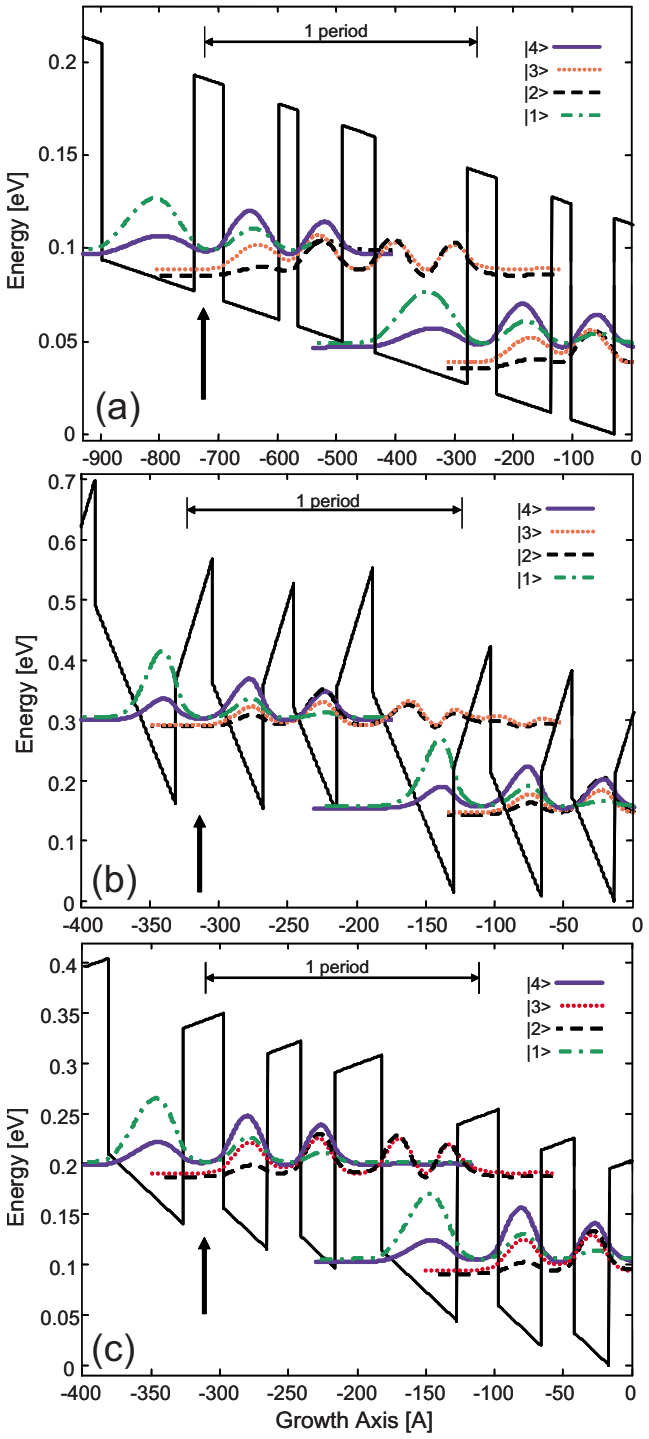

FIG. 2. (Color online) Conduction-band profile and squared envelope functions of (a) the GaAs/$Al_{0.15}Ga_{0.85}As$, (b) the GaN/$Al_{0.15}Ga_{0.85}N$, and (c) the ZnO/$Mg_{0.15}Zn_{0.85}O$ QC gain media considered in this study.

target emission frequency of 2 THz (8.2 meV), chosen because it lies in a window of relatively high atmospheric transmission within the terahertz spectrum.

The conduction-band diagrams of Fig. 2 were computed by solving the following Schrödinger equations, Eq. (1) and Eq. (2), in the well and barrier layers, respectively, together with standard boundary conditions of quantum mechanics:

$$\left[-\frac{\hbar^2}{2m_c^w}\frac{d^2}{dz^2}+e(F_{ext}+F_{int}^w)z\right]\phi(z)=E\phi(z), \quad (1)$$

TABLE I. Summary of the material parameters used in the simulations presented in this work. The superscripts *w* and *b* denote the well and barrier material, respectively.

	GaAs/ $Al_{0.15}Ga_{0.85}As$	GaN/ $Al_{0.15}Ga_{0.85}N$	ZnO/ $Mg_{0.15}Zn_{0.85}O$
m_c^w	0.067	0.20	0.24
m_c^b	0.079	0.22	···
ϵ_s^w	13.18	10.28	8.1
ϵ_s^b	12.71	10.28	···
ϵ_∞^w	10.89	5.29	4.11
ΔE_c (meV)	116	207	208
ΔP (C m^{-2})	0	0.012	0.0014
$\hbar\omega_{LO}^w$ (meV)	36.25	91.2	72.0

$$\left[-\frac{\hbar^2}{2m_c^b}\frac{d^2}{dz^2}+\Delta E_c+e(F_{ext}+F_{int}^b)z\right]\phi(z)=E\phi(z). \quad (2)$$

The resulting eigenvalues E are the conduction subband minima of the QC structure under study, and the associated envelope functions are given by the corresponding solutions for $\phi(z)$. In Eqs. (1) and (2), m_c^w and m_c^b are the electronic effective masses of the well and barrier material, respectively, e is the electron charge, ΔE_c is the QW conduction-band offset, F_{ext} is the electric field due to the externally applied voltage bias, and F_{int} is the intrinsic electric field due to spontaneous and piezoelectric polarizations.

The latter electric field is zero in (001) GaAs/AlGaAs QWs. On the other hand, it can be quite large in GaN/AlGaN and ZnO/MgZnO QWs grown on *c*-plane substrates, due to the symmetry of their wurtzite crystal structure and to their relatively high degree of strain. In these QWs, strong spontaneous and piezoelectric polarizations exist along the growth direction (P_{sp} and P_{pz}), whose discontinuities at each heterojunction lead to large densities of interface charge. The electric fields produced by these sheet charge distributions can be computed using simple electrostatic arguments (i.e., by requiring conservation of the electric displacement flux across each interface) together with an appropriate set of boundary conditions.[21,22] The Schrödinger solver used in this work employs periodic boundary conditions,[23] for which the intrinsic voltage drop across each QC repeat unit is required to be zero. This is appropriate for thick gain media consisting of several such periods, and leads to the following expression for the internal field in each epitaxial layer:

$$F_{int,j}=\frac{\Sigma_{k\neq j}(P_k-P_j)\dfrac{L_k}{\varepsilon_{s,k}}}{\varepsilon_{s,j}\Sigma_k\dfrac{L_k}{\varepsilon_{s,k}}}, \quad (3)$$

where the subscripts j and k refer to the layer number, the summations run over all layers in one repeat unit, L denotes the layer thickness, ε_s the static permittivity, and $P=P_{sp}+P_{pz}$ the total polarization which depends on the layer alloy composition and elastic strain.

The numerical values used for the relevant material parameters of the QWs under study are listed in Table I. In the case of the GaAs/AlGaAs system, these values are well established and can be found, e.g., in Refs. 24 and 25. Extensive literature is also available regarding the key material parameters of GaN/AlGaN QWs, although discrepancies still exist in some cases. Here we follow the recommendations of Ref. 26 for all band parameters, including those needed to compute $\Delta P=P_w-P_b$, of Ref. 23 for the dielectric constants and of Ref. 27 for the phonon energy. Finally, the values listed in Table I for the ZnO/MgZnO QW system were taken from Refs. 28 and 29 (ΔE_c), Ref. 30 (ΔP), and Ref. 31 (all other parameters). The available information about MgZnO is particularly sparse at this stage, leading to a number of missing entries in the table for which the corresponding values of ZnO were used. We expect that this is a reasonable approximation given the relatively low Mg content in the case under study (15%).

Finally, it should be noted that the piezoelectric polarizations P_{pz}, and hence the overall polarization discontinuity ΔP, depend on the degree of strain in the well and barrier layers, which in turn is determined by the growth substrate used. In the case of the GaN QC structures, ΔP was computed with the procedure described, e.g., in Ref. 21 assuming pseudomorphic growth on an $Al_{0.07}Ga_{0.93}N$ strain-balancing template. In the case of the ZnO gain medium, it was extrapolated from the results of Ref. 30 where a template of the same composition as the barrier layers was used. Given the rather small value of ΔP in these ZnO/$Mg_{0.15}Zn_{0.85}O$ QWs, we expect that use of a strain-balancing template (which is more favorable from a material structural quality standpoint) would not affect the results of these simulations in any appreciable way.

III. MONTE CARLO SIMULATION MODEL

Our model relies on a particle-based Monte Carlo approach to determine the steady-state carrier distributions of the laser subbands as a function of temperature, starting from a constant population initially assigned to each subband. This approach has been already applied to study the carrier dynamics and the population inversion characteristics in other QC structures.[2,32–34] Typically several thousand particles per subband are simulated, and specifically the results presented in Sec. IV have been obtained using an ensemble of 5000 electrons per subband. Initially the particles are assigned in equal number to each subband according to a thermal distribution. The ensemble is subsequently allowed to evolve and the simulation is terminated when the population of each subband remains unchanged for a given number of iteration steps. The convergence is checked both with respect to each subband within a single repeat unit and between identical subbands in different repeat units. Each iteration step involves a number of subhistories in which the state of each particle evolves for a given time and the distribution-function-based statistics are updated.

The numerical model for the device structures studied in this work includes 4 subbands per period, and 3 adjacent periods are simulated for a total of 12 subbands. Periodic boundary conditions are applied such that for each particle exiting the third repeat unit, a new one is injected in the first.

Electron/electron and electron/LO-phonon scattering are both included in the simulations[35–37] with the relevant scattering rates at a given temperature computed and stored for each subband pair for a discrete number of initial electron k-vectors (energies). For the structures presented in this work 200 k-steps have been used to describe the scattering rates, corresponding to a maximum energy up to 0.75 eV. During the Monte Carlo simulation, an interpolation is used to determine the rates at arbitrary initial energy values. The same procedure is used to evaluate and store the form factors for both electron/LO-phonons and electron/electron interactions. The electron/LO-phonon scattering rates are evaluated for each temperature during the Monte Carlo run. When convergence is reached, the populations of the relevant subbands are computed and used to determine the inversion.

A. LO-phonon scattering

The two-dimensional (2D) electron/LO-phonon scattering rate between subbands ν and ν' is given by[35,38]

$$\frac{1}{\tau^{\mathrm{LO}}_{\nu\nu'}(\vec{k}_i)} = \frac{m_c e^2 \hbar \omega_{\mathrm{LO}}}{8\pi\hbar^3 \varepsilon_0}\left(\frac{1}{\varepsilon_\infty} - \frac{1}{\varepsilon_s}\right) \times \left[N_{\mathrm{LO}} \int_0^{2\pi} S_{\nu\nu'}(\vec{q}_{\mathrm{abs}}) d\theta + (N_{\mathrm{LO}}+1) \int_0^{2\pi} S_{\nu\nu'}(\vec{q}_{\mathrm{emi}}) d\theta \right], \tag{4}$$

where m_c is the electron effective mass, $\hbar\omega_{\mathrm{LO}}$ is the longitudinal optical phonon energy, and ε_∞ and ε_s are the high-frequency and static dielectric constants, respectively. For all these parameters, the values of the well materials were used in the following for simplicity. The first integral on the right-hand side of Eq. (4) accounts for the absorption while the second for the emission of LO-phonons. N_{LO} is the average phonon number. The argument in both integrals of Eq. (4) is given by

$$S_{\nu,\nu'}(\vec{q}) = \frac{H_{\nu\nu'}(\vec{q})}{\sqrt{q^2+q_s^2}} = \int_{-\infty}^{\infty} dz \int_{-\infty}^{\infty} dz' \rho_{\nu\nu'}(z) \rho^*_{\nu\nu'}(z') I(q,q_s,z,z'), \tag{5}$$

where q_s is the inverse screening length and $\rho_{\nu\nu'}(z) = \phi_\nu(z)\phi_{\nu'}(z)$, with the subband envelope functions $\phi_\nu(z)$ obtained from Eqs. (1) and (2). The quantity $I(q,q_s,z,z')$ is given by

$$I(q,q_s,z,z') = \frac{e^{-(\sqrt{q^2+q_s^2}|z-z'|)}}{\sqrt{q^2+q_s^2}} \times \left[1 - \frac{|z-z'|q_s^2}{2\sqrt{q^2+q_s^2}} - \frac{q_s^2}{2(q^2+q_s^2)} \right]. \tag{6}$$

In this work we employ the zero screening limit $q_s \to 0$, for which Eq. (5) becomes

$$\frac{H_{\nu\nu'}(\vec{q})}{\vec{q}} = \frac{1}{q}\int_{-\infty}^{\infty} dz \int_{-\infty}^{\infty} dz' \rho_{\nu\nu'}(z) \rho^*_{\nu\nu'}(z') e^{-(q|z-z'|)}. \tag{7}$$

Based on the requirement of energy and momentum conservation, the magnitude of the exchanged wavevector q is given by

$$q = \sqrt{2k_\nu^2 - 2\frac{m_c \Delta E}{\hbar^2} - 2k_\nu \cos\theta \sqrt{k_\nu^2 - 2\frac{m_c \Delta E}{\hbar^2}}}, \tag{8}$$

where θ is the angle between the initial ($\vec{k}_\nu$) and final ($\vec{k}_{\nu'}$) electron k-vectors and the quantity ΔE depends on the type of scattering. Specifically, for an absorption process we have $\Delta E_{\mathrm{abs}} = E_{\nu'} - E_\nu - \hbar\omega_{\mathrm{LO}}$ while for an emission $\Delta E_{\mathrm{emi}} = \hbar\omega_{\mathrm{LO}} + E_{\nu'} - E_\nu$. Consequently, Eq. (5) is a function of the type of process (absorption or emission), the scattering angle and the initial electron k-vectors. In other words,

$$\frac{H_{\nu\nu'}(\vec{q})}{\sqrt{q^2+q_s^2}} \to \begin{bmatrix} \dfrac{H_{\nu\nu'}[\vec{q}_{\mathrm{abs}}(\vec{k}_\nu,\theta)]}{\sqrt{[q_{\mathrm{abs}}(\vec{k}_\nu,\theta)]^2+q_s^2}} \\ \dfrac{H_{\nu\nu'}[\vec{q}_{\mathrm{emi}}(\vec{k}_\nu,\theta)]}{\sqrt{[q_{\mathrm{emi}}(\vec{k}_\nu,\theta)]^2+q_s^2}} \end{bmatrix}. \tag{9}$$

Figure 3 presents the calculated LO-phonon emission rates from subbands $|4\rangle$ [Fig. 3(a)] and $|3\rangle$ [Fig. 3(b)] of the nth repeat unit to all the subbands in the same repeat unit for the GaN QC structure of Fig. 2(b). In both plots, the horizontal axis corresponds to the energy of the initial states, and the zero-energy reference value is taken at the bottom of subband $|4\rangle_n$ and $|3\rangle_n$, respectively. It should be noted how the LO-phonon scattering rate from the bottom of subband $|4\rangle$ is about two orders of magnitude lower than from the bottom of subband $|3\rangle$. This is a key feature of the resonant-phonon terahertz QC design, which ensures high-gain operation as long as most electrons in $|4\rangle$ reside near the bottom of the subband.

In the course of the Monte Carlo simulation, the final state of each electron in its selected final subband is obtained by determining the scattering angle using a direct rejection technique applied to the integrand of Eq. (4). Specifically, the expressions in Eq. (9) are precomputed for each pair of subbands on a grid of values of the angle θ and the initial electron wavenumber k_i (equivalently the energy E_i), for both absorption and emission processes using Eq. (8). Figure 4 presents the calculated values of $H_{11}[q_{\mathrm{emi}}(\vec{k}_i,\theta)]/\sqrt{[q_{\mathrm{emi}}(\vec{k}_i,\theta)]^2+q_s^2}$ for the intraband LO-phonon emission process in the first subband of the nth repeat unit, as a function of θ and for different values of E_i. This 2D data set is used as a lookup table in the direct rejection method[39] to obtain the scattering angle. The final state is subsequently obtained using energy and momentum conservation.

B. Electron-electron scattering

Regarding the electron/electron interaction, we consider the scattering of a primary electron with wavevector $\vec{k}$ in subband ν with a secondary one with wavevector $\vec{p}$ in subband μ. The final states of the two particles are labeled by

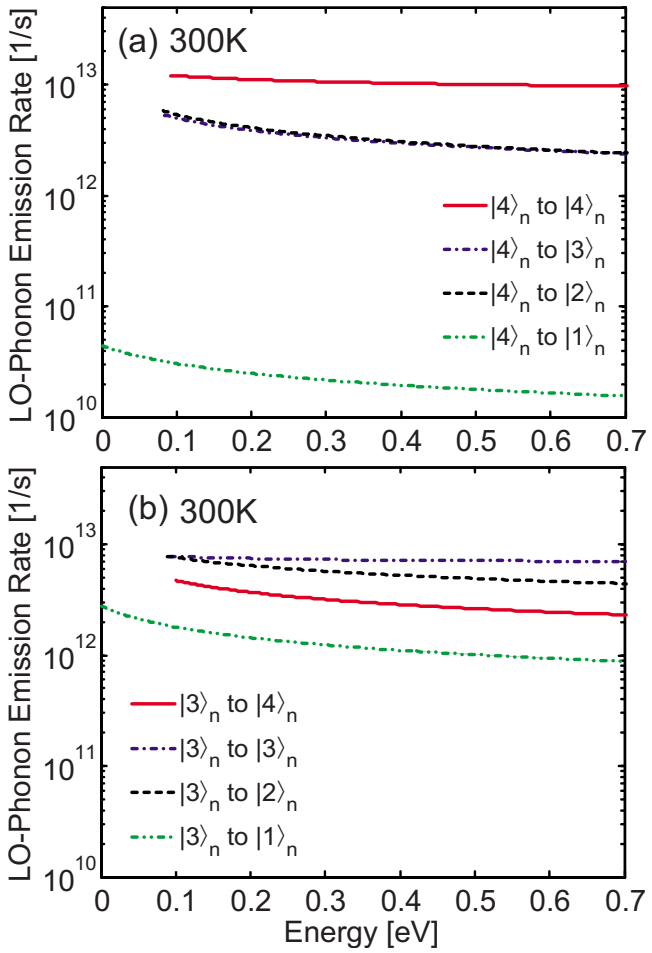

FIG. 3. (Color online) Calculated LO-phonon emission rate from subbands $|4\rangle$ (a) and $|3\rangle$ (b) to all the subbands in the same repeat unit for the GaN QC structure of Fig. 2(b) at an operating temperature of 300 K. In the horizontal axes, energy is measured from the bottom of subbands $|4\rangle$ and $|3\rangle$, respectively.

the subband indices ν', μ' and wavevectors $\vec{k}', \vec{p}'$. Using Fermi's golden rule the electron-electron scattering rate can be evaluated as[34,37]

$$\frac{1}{\tau^{ee}_{\nu\nu'}(\vec{k})} = \frac{m_c}{4\hbar^3 \pi A} \sum_{\mu\mu'\vec{p}} f_\mu(\vec{p}) \int_0^{2\pi} |M_{\nu\mu\nu'\mu'}(\vec{q})|^2 d\theta, \tag{10}$$

where $\vec{q}=\vec{k}-\vec{k}'$, A is the sample area, and θ is the angle between the vectors $\vec{p}-\vec{k}$ and $\vec{p}'-\vec{k}'$. $M_{\nu\mu\nu'\mu'}(\vec{q})$ is the matrix element that describes the interaction, which is computed as in Ref. 34, and $f_\mu(\vec{p})$ is the secondary electron distribution. Because this distribution is not known beforehand, a rejection technique is normally employed to determine the correct scattering rate.[34,35] To be able to use the rejection technique, an upper bound of the scattering rate expressed by Eq. (10) has to be found. First, we determine a constant value $M_{\nu\mu\nu'\mu'}$ that is the maximum matrix element for the interaction process between electrons in the subbands $\nu\mu\nu'\mu'$. Introducing the 2D carrier density n_μ of the secondary electron subband, the maximum scattering rate value is

$$\left.\frac{1}{\tau^{ee}_{\nu\nu'}(\vec{k})}\right|_{\max} = \frac{m_c}{2\hbar^3} \sum_{\mu\mu'} n_\mu M^2_{\nu\mu\nu'\mu'}. \tag{11}$$

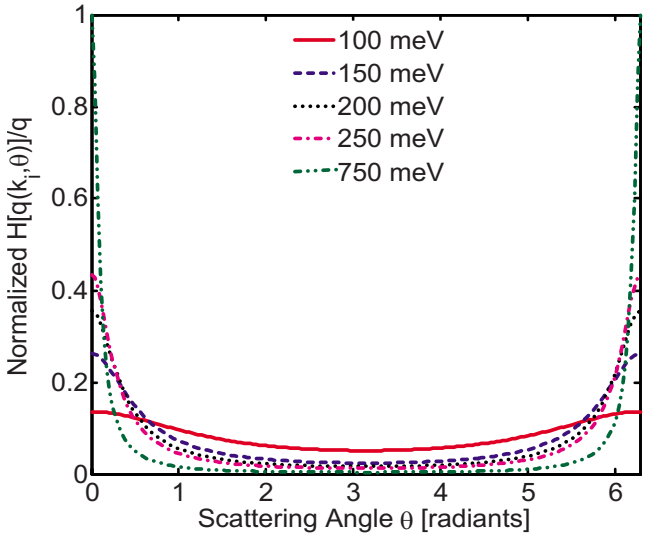

FIG. 4. (Color online) Calculated values from expression (9) for the intraband LO-emission process in the first subband of the nth repeat unit as a function of the scattering angle θ and initial electron energy.

During the Monte Carlo calculation, if an electron-electron interaction is selected, the final subband ν' is determined by the relative magnitude of half[37] the rate computed by Eq. (11). The secondary electron is selected randomly from the particle ensemble and its final subband is determined by the magnitude of the coefficient $M_{\nu\mu\nu'\mu'}$ with $\nu\mu\nu'$ fixed. The Coulomb interaction potential used to evaluate the matrix element $M_{\nu\mu\nu'\mu'}(\vec{q})$ as in Ref. 34 is

$$V_{\nu\mu\nu'\mu'}(\vec{q}) = \frac{e^2}{2\varepsilon_s} \frac{A_{\nu\mu\nu'\mu'}(\vec{q})}{q\varepsilon_{\rm scr}(\vec{q})}, \tag{12}$$

where

$$A_{\nu\mu\nu'\mu'}(\vec{q}) = \int_{-\infty}^{\infty} dz \int_{-\infty}^{\infty} dz' \rho_{\nu\nu'}(z) e^{-q|z-z'|} \rho^*_{\mu\mu'}(z'). \tag{13}$$

The interaction form factors $A_{\nu\mu\nu'\mu'}(\vec{q})$ given by Eq. (13) are precomputed for each subband combination for a set of discrete values of q-vectors and stored along with the maximum value to be used for the rejection procedure. The screening factor $\varepsilon_{\rm scr}(\vec{q})$ is evaluated under the single-subband approximation[40] using the following equation:

$$\varepsilon_{\rm scr}(\vec{q}) = 1 + \frac{e^2}{2\varepsilon_s \vec{q}} A_{\nu\mu\nu'\mu'}(\vec{q}) \Pi_\nu(\vec{q}). \tag{14}$$

In the long-wave approximation, the diagonal elements $\Pi_\nu(q)$ of the polarizability tensor are given by[34]

$$\Pi_\nu(q \to 0) = -\frac{m_c}{\pi\hbar^2} f_\nu(0) = -\frac{m_c}{\pi\hbar^2}[1 - e^{n_\nu \pi\hbar^2/m_c k_B T^e_\nu}], \tag{15}$$

where n_ν is the carrier density and T^e_ν is the electron temperature of subband ν. The latter parameter, which in general is different from the lattice temperature, is computed directly from the carrier distribution during the Monte Carlo calculation.

Lee and Galbraith[41] pointed out that the single-subband approximation may introduce errors in the interaction matrix elements. Although Bonno *et al.*[34] proposed a computationally efficient approach to mitigate this problem, in general the solution of the full screening matrix should be carried out. Furthermore Mošková and Mosko[42] suggested that Fermi's golden rule tends to overestimate the carrier-carrier scattering rate compared to the results of a more rigorous phase shift analysis, especially in the case of GaN (as opposed to GaAs) 2D systems. The investigation of these effects in the present context will require the development of additional computationally efficient models to be included in our numerical simulator and will be the subject of future studies. In any case, it should be noted that in the QC structures of Fig. 2 the main role of electron-electron scattering is to depopulate the upper laser states (whereas the lower laser states are mainly depopulated via LO-phonon emission). Thus, an overestimate of this scattering process in the GaN device would if anything lead to an underestimate of its performance improvements over the GaAs structure.

Recently, a number of research groups have also investigated hot-phonon effects in GaN.[43–46] This has been motivated by the consideration that, because of the large LO-phonon emission rate in GaN, the optical phonon population could be significantly far from equilibrium. The majority of this work has been carried out for 2D electron gas systems in GaN/AlGaN heterostructures where the transport in the channel was studied. It is not clear at this point what kind of impact, if any, the hot-phonon effect could have on the type of QC structures studied in this work. In fact, the latter are significantly different from the conventional heterostructure field effect transistor (HFET) device structure in which these phenomena have been observed. Furthermore, the carrier densities in our devices are three orders of magnitude lower than the density of electrons in the GaN/AlGaN HFETs that were the subjects of these hot-phonon investigations. Lu and Cao[32] studied the same problem in conventional GaAs/AlGaAs QC-laser structures and argued that while the device current changes significantly as a result of the presence of hot phonons, the population inversion remains almost unchanged. It is not clear if these findings are valid also for GaN and ZnO based QC lasers and further investigation is necessary to clarify this issue.

IV. SIMULATION RESULTS

Using the simulation model just described we have calculated the steady-state carrier distributions of the three QC structures under study as a function of the operating temperature. To illustrate, in Figs. 5(a) and 5(b) we plot the normalized number density functions (NDFs) (defined as the product of the nonequilibrium distribution function and the density of states) of the upper $|4\rangle$ and lower $|3\rangle$ laser states of the GaAs and GaN structures, at temperatures of 100 and 200 K, respectively. From these figures, it can be immediately noticed that the ratio between the NDFs of the upper and lower laser subbands at a given energy is always greater in the GaN device than in the GaAs structure. Furthermore, at 100 K [Fig. 5(a)] the NDF of the GaN and GaAs upper laser levels become very small at energies around 90 and 35 meV above the subband minimum, respectively, which correspond to the thresholds for LO-phonon emission in these materials. As the operating temperature is increased to 200 K [Fig. 5(b)], the upper- and lower-laser-level NDFs of the GaN structure do not change substantially, except for a small shift of carriers toward higher energies in the upper subband. On the other hand, the NDFs of the GaAs structure present a significant increase in the population of the lower laser level and a larger number of carriers in the higher energy states above the LO-phonon energy for both levels. This is due to the backfilling effect associated with LO-phonon absorption, which in GaAs becomes more and more probable as the temperature is increased compared to GaN. Furthermore, in the GaAs structure at higher and higher temperatures the ratio between the NDFs of the upper and lower laser levels decreases and the population inversion eventually falls below the threshold needed for lasing.

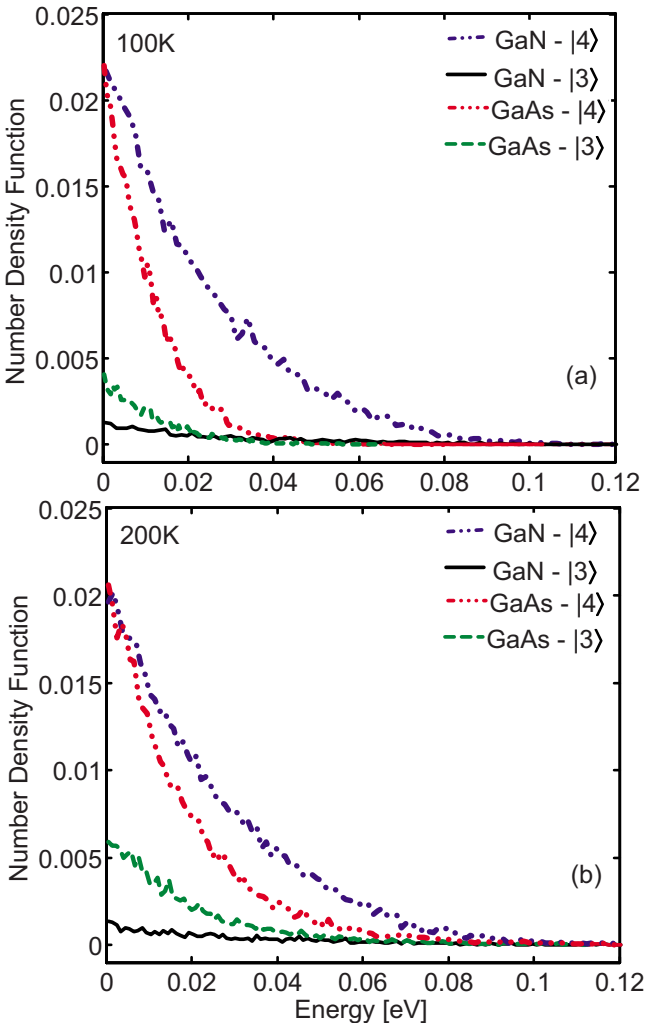

FIG. 5. (Color online) Calculated NDF of the upper $|4\rangle$ and lower $|3\rangle$ laser states of the GaAs and GaN structures at temperatures of 100 K (a) and 200 K (b).

It should be mentioned that during the Monte Carlo run the carrier distribution is monitored to detect electron escape from the confined states. Specifically, when a particle reaches an energy state above the maximum conduction-band edge of the barrier downstream it is removed from the simulation.

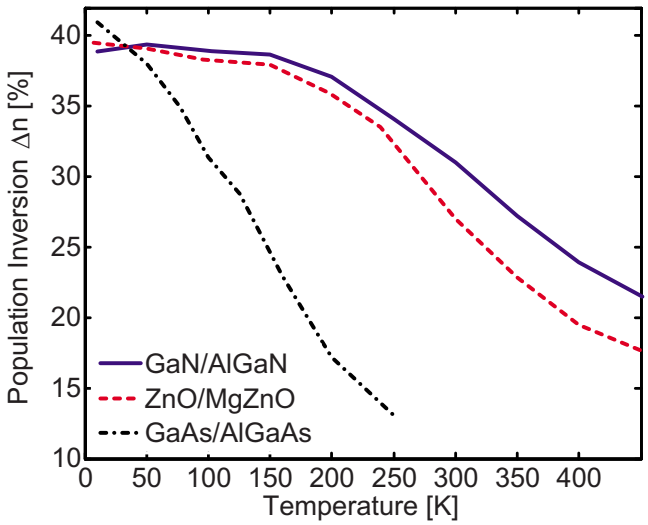

FIG. 6. (Color online) Calculated fractional population inversion of the terahertz QC structures of Fig. 2(a) (dash-dot line), Fig. 2(b) (solid line), and Fig. 2(c) (dashed line), as a function of temperature.

Although in practice these carriers will be eventually recaptured by different wells, their removal is intended to represent a worst case scenario for the device operation. In any case we have found that these escape processes have negligible effect up to room temperature. Thus, they do not play a role in determining the maximum operating temperature of the GaAs device, nor they effect the claim made below that the GaN and ZnO structures can operate without cryogenic cooling.

Finally, Fig. 6 presents the calculated fractional population inversion $\Delta n=(n_4-n_3)/n_{\mathrm{tot}}$ versus temperature for the three structures of Figs. 2(a)–2(c). Here, n_4 and n_3 are the sheet electron densities of the upper and lower laser subbands, as computed from their respective NDFs, and n_{tot} is the total electron density per period, which in this calculation has been taken to be 2×10^{10} cm^{-2}. The results plotted in this figure fully support and quantify the claim that GaN and ZnO terahertz QC structures can provide better performance compared to GaAs gain media.

In particular, Δn in the former two structures is found to degrade much more slowly with increasing temperature compared to the GaAs device. For example, as the temperature is increased from 10 to 300 K, Δn in the GaN and ZnO structures decreases only by factors of 1.25 and 1.50, respectively, versus 4.48 in the GaAs gain medium. The latter result is consistent with the severe performance degradation with increasing temperature experimentally observed in GaAs terahertz QC lasers, which is caused by thermally activated LO-phonon emission and (to a lesser extent[6]) by thermal backfilling of the lower laser states from the states downstream. Both of these limiting factors are much less effective in the presence of the large LO-phonon energies of GaN/AlGaN and ZnO/MgZnO QWs, as clearly indicated by our simulation results.

The maximum operating temperatures of the three gain media can be estimated from the plots of Fig. 6 as the temperatures beyond which Δn is smaller than the population inversion required to reach laser threshold. In QC lasers, the latter quantity can be written as follows:[47]

$$\Delta n_{\mathrm{th}}=\frac{1}{n_{\mathrm{tot}}}\frac{\alpha\varepsilon_o\eta c\gamma L_p}{\Gamma N_p\omega(qz)^2}, \tag{16}$$

where η is the refractive index, γ is the full width at half maximum of the gain spectrum, L_p is the length of one period of the active material, Γ is the optical confinement factor per period, N_p is the number of periods, $\hbar\omega$ is the energy of the emitted photons, α is the total cavity loss coefficient, and qz is the electric dipole moment of the laser transition. From the simulation results shown in Figs. 2(a)–2(c), we have $L_p=462$ Å and $z=66$ Å for the GaAs structure, $L_p=199$ Å and $z=30$ Å for the ZnO structure, and $L_p=201$ Å and $z=33$ Å for the GaN structure. In all three devices, $n_{\mathrm{tot}}=2\ 10^{10}$ cm^{-2} and $\hbar\omega=8.2$ eV by design. Incidentally, with this set of parameters the oscillator strengths are computed to be 0.63 in the GaAs gain medium and 0.47 in both the GaN and the ZnO structures. For the refractive indices near 2 THz, we use the experimentally determined values of 3.8, 2.8, and 3 for GaAs, ZnO, and GaN, respectively.[48–50] Furthermore, from previously reported measurements with GaAs terahertz-QC-laser waveguides based on surface plasmons,[5,8] we take $\alpha/\Gamma N_p=20$ cm^{-1} for all three structures considered here.

Regarding the gain linewidth γ, a typical value for the GaAs device under study extrapolated from the literature is 3 meV.[48] This can be ascribed partly to lifetime broadening (given the ultrafast, ~100 fs, phonon-assisted depopulation of the lower laser states) and partly to broadening due to surface roughness. Using this value in Eq. (16), we calculate for the GaAs structure of Fig. 2(a) a minimum population inversion required to achieve lasing $\Delta n_{\mathrm{th}}=16\%$. The maximum operating temperature correspondingly obtained from the simulation results of Fig. 6 is $T_{\mathrm{max}}\approx200$ K. This value is reasonably close to the largest working temperature reported to date with GaAs devices, approximately 170 K,[5] indicating that our model accurately describes the temperature dependent performance of terahertz QC lasers.

If the same linewidth of 3 meV is assumed for the GaN structure of Fig. 2(b), a threshold population inversion of $\Delta n_{\mathrm{th}}=22\%$ and a maximum operating temperature of over 400 K are obtained. Similarly, if we assume $\gamma=3$ meV in the ZnO QC gain medium of Fig. 2(c), we obtain $\Delta n_{\mathrm{th}}=25\%$ and T_{max} over 300 K. Furthermore, the ability of these devices to operate without cryogenic cooling (i.e., at temperatures accessible with thermoelectric coolers, >250 K) is predicted for linewidths up to over 4.6 and 3.8 meV for the GaN and ZnO structures, respectively. Incidentally, in this analysis we have neglected the temperature dependence of the gain linewidth for simplicity. In any case, this dependence can be expected to be relatively small, again because of the large LO-phonon energies of these materials.

Experimentally, while no measurements at terahertz frequencies have yet been reported, near-infrared ISB photoluminescence peaks with relatively large quality factors $\hbar\omega/\gamma$ have been obtained in narrower and more highly strained GaN/AlN QWs (Refs. 13 and 16) (e.g., 60 meV linewidth for emission near 580 meV in Ref. 13). In these systems, the ISB transition linewidths are typically dominated by interface roughness scattering, whose contribution to the quality factor $\hbar\omega/\gamma$ tends to increase with increasing well width.[51]

Thus, nitride terahertz QC structures with sufficiently low ISB linewidths are expected to be feasible. In the case of ZnO/MgZnO QWs, the available experimental data are currently too limited to make similar predictions. We point out, however, that the generally smaller lattice mismatch and strain featured by these heterostructures compared to nitride QWs are promising in this respect.

V. CONCLUSIONS

In summary, we have presented a rigorous Monte Carlo study of carrier dynamics versus temperature in three otherwise identical terahertz QC structures based on GaAs/AlGaAs, ZnO/MgZnO, and GaN/AlGaN QWs. The simulation results clearly indicate that the latter two materials systems are promising to dramatically improve the high-temperature performance of terahertz injection lasers. In particular, as the temperature is increased from 10 to 300 K, the population inversion and hence the optical gain are found to decrease by factors of 4.48, 1.50, and 1.25 for the AlGaAs, MgZnO, and AlGaN structures, respectively. These predictions bear out and quantify the expectation that the larger the LO-phonon energies (as in going from the AlGaAs to the MgZnO to the AlGaN materials system), the more robust the population inversion with respect to thermally activated nonradiative ISB scattering. Furthermore, the simulation results suggest that the GaN and ZnO QC structures considered in this work can provide lasing without cryogenic cooling if their gain linewidths are smaller than about 4.6 and 3.8 meV, respectively. While these values appear to be feasible, the growth and experimental demonstration of both structures remain a considerable challenge, particularly with regard to obtaining efficient tunneling-based interwell transport. On the other hand, the prospect of operation without cryogenic cooling suggested by this study has the potential for a revolutionary impact in the general field of terahertz photonics, and should therefore provide strong impetus for the investigation of these devices.

ACKNOWLEDGMENTS

This work has been supported by the NSF through Grant No. ECCS-0824116.

[1]M. Lee and M. C. Wanke, Science **316**, 64 (2007).
[2]R. Köhler, A. Tredicucci, F. Beltram, H. E. Beere, E. H. Linfield, A. G. Davies, D. A. Ritchie, R. C. Iotti, and F. Rossi, Nature (London) **417**, 156 (2002).
[3]*Intersubband Transitions in Quantum Structures* 1st ed., edited by R. Paiella (McGraw-Hill, New York, 2006).
[4]G. Scalari, L. Ajili, J. Faist, H. Beere, E. Linfield, D. Ritchie, and G. Davies, Appl. Phys. Lett. **82**, 3165 (2003).
[5]B. S. Williams, S. Kumar, Q. Hu, and J. L. Reno, Opt. Express **13**, 3331 (2005).
[6]B. S. Williams, S. Kumar, Q. Qin, Q. Hu, and J. L. Reno, Appl. Phys. Lett. **88**, 261101 (2006).
[7]H. Luo, S. R. Laframboise, Z. R. Wasilewski, G. C. Aers, H. C. Liu, and J. C. Cao, Appl. Phys. Lett. **90**, 041112 (2007).
[8]C. Walther, M. Fischer, G. Scalari, R. Terazzi, N. Hoyler, and J. Faist, Appl. Phys. Lett. **97**, 131122 (2007).
[9]C. Gmachl, H. M. Ng, and A. Y. Cho, Appl. Phys. Lett. **77**, 334 (2000).
[10]D. Hofstetter, S.-S. Schad, H. Wu, W. J. Schaff, and L. F. Eastman, Appl. Phys. Lett. **83**, 572 (2003).
[11]L. Nevou, M. Tchernycheva, L. Doyennette, F. H. Julien, E. Warde, R. Colombelli, F. Guillot, S. Leconte, E. Monroy, T. Remmele, and M. Albrecht, Superlattices Microstruct. **40**, 412 (2006).
[12]N. Iizuka, K. Kaneko, and N. Suzuki, IEEE J. Quantum Electron. **42**, 765 (2006).
[13]L. Nevou, M. Tchernycheva, F. H. Julien, F. Guillot, and E. Monroy, Appl. Phys. Lett. **90**, 121106 (2007).
[14]K. Driscoll, A. Bhattacharyya, T. D. Moustakas, R. Paiella, L. Zhou, and D. J. Smith, Appl. Phys. Lett. **91**, 141104 (2007).
[15]Y. Li, A. Bhattacharyya, C. Thomidis, T. D. Moustakas, and R. Paiella, Opt. Express **15**, 17922 (2007).
[16]K. Driscoll, Y. Liao, A. Bhattacharyya, L. Zhou, D. Smith, T. Moustakas, and R. Paiella, Appl. Phys. Lett. **94**, 081120 (2009).
[17]V. D. Jovanović, D. Indjin, Z. Ikonić, and P. Harrison, Appl. Phys. Lett. **84**, 2995 (2004).
[18]G. Sun, R. A. Soref, and J. B. Khurgin, Superlattices Microstruct. **37**, 107 (2005).
[19]E. Bellotti, K. Driscoll, T. D. Moustakas, and R. Paiella, Appl. Phys. Lett. **92**, 101112 (2008).
[20]M. Belmoubarik, K. Ohtani, and H. Ohno, Appl. Phys. Lett. **92**, 191906 (2008).
[21]O. Ambacher, B. Foutz, J. Smart, J. R. Shealy, N. G. Weimann, K. Chu, M. Murphy, A. J. Sierakowski, W. J. Schaff, L. F. Eastman, R. Dimitrov, A. Mitchell, and M. Stutzmann, J. Appl. Phys. **87**, 334 (2000).
[22]S. Gunna, F. Bertazzi, R. Paiella, and E. Bellotti, in *Nitride Semiconductor Devices: Principles and Simulation*, edited by J. Piprek (Wiley-VCH, Berlin, 2007), pp. 117–143.
[23]B. K. Ridley, W. J. Schaff, and L. F. Eastman, J. Appl. Phys. **94**, 3792 (2003).
[24]S. Adachi, J. Appl. Phys. **58**, R1 (1985).
[25]*Semiconductors: Basic Data* edited by O. Madelung (Springer-Verlag, Berlin, 1996).
[26]A. Vurgaftman and J. Meyer, J. Appl. Phys. **94**, 3675 (2003).
[27]N. E. Christiansen and P. Perlin, in *Gallium Nitride I*, edited by J. I. Pankove and T. D. Moustakas, 1st ed. (Academic Press, San Diego, CA, 1998), pp. 409–430.
[28]A. Ohtomo, M. Kawasaki, T. Koida, K. Masubuchi, H. Koinuma, Y. Sakurai, Y. Yoshida, T. Yasuda, and Y. Segawa, Appl. Phys. Lett. **72**, 2466 (1998).
[29]A. P. Abiyasa, S. F. Yu, W. J. Fan, and S. P. Lau, IEEE J. Quantum Electron. **42**, 455 (2006).
[30]S. H. Park and D. Ahn, Appl. Phys. Lett. **87**, 253509 (2005).
[31]G. Coli and K. K. Bajaj, Appl. Phys. Lett. **78**, 2861 (2001).
[32]J. Lu and J. Cao, Appl. Phys. Lett. **88**, 061119 (2006).
[33]C. Jirauschek, G. Scarpa, P. Lugli, M. Vitiello, and G. Scamarcio, Appl. Phys. Lett. **101**, 086109 (2007).
[34]O. Bonno, J.-L. Thobel, and F. Dessenne, J. Appl. Phys. **97**, 043702 (2005).
[35]S. M. Goodnick and P. Lugli, Phys. Rev. B **37**, 2578 (1988).
[36]M. Mosko and A. Moskova, Phys. Rev. B **44**, 10794 (1991).
[37]M. Mosko, A. Moskova, and V. Cambel, Phys. Rev. B **51**, 16860 (1995).
[38]J. H. Smet, C. G. Fonstad, and Q. Hu, Phys. Rev. B **79**, 009305 (1996).
[39]C. Jacoboni and P. Lugli, *The Monte Carlo Method for Semiconductor Device Simulation*, Computational Microelectronics (Springer-Verlag, Wien, 1989).
[40]P. Harrison, *Quantum Wells Wires and Dots* (Wiley, New York, 2002).
[41]S.-C. Lee and I. Galbraith, Phys. Rev. B **59**, 15805 (1999).
[42]A. Moskova and M. Mosko, Phys. Rev. B **61**, 3048 (2000).
[43]K. Wang, J. Simon, N. Goel, and D. Jena, Appl. Phys. Lett. **88**, 022103 (2006).
[44]G. Xu, S. Tripathy, X. Mu, Y. Ding, K. Wang, Y. Cao, D. Jena, and J. Khurgin, Appl. Phys. Lett. **93**, 051912 (2008).
[45]J. Khurgin, Y. Ding, and D. Jena, Appl. Phys. Lett. **91**, 252104 (2007).
[46]M. Ramonas, A. Matulionis, J. Liberis, L. Eastman, X. Chen, and Y.-J. Sun, Phys. Rev. B **71**, 075324 (2005).
[47]C. Sirtori and R. Teissier, in *Intersubband Transitions in Quantum Structures*, edited by R. Paiella (McGraw-Hill, New York, 2006), pp. 1–39.
[48]H. Callebout, S. Kumar, B. S. Williams, Q. Qin, Q. Hu, and J. L. Reno, Appl. Phys. Lett. **83**, 207 (2003).
[49]W. Zhang, A. K. Azad, and D. Grischkowsky, Appl. Phys. Lett. **82**, 2841 (2003).
[50]J. Han, Z. Zhu, S. Ray, A. K. Azad, W. Zhang, and M. He, Appl. Phys. Lett. **89**, 031107 (2006).
[51]M. Helm, in *Intersubband Transitions in Quantum Wells: Physics and Device Applications I*, edited by H. C. Liu and F. Capasso (Academic, New York, 2000), pp. 1–100.